Secondary Rare Earth Element (REE) Mineralization in a Skarn Regolith, Doradilla, NSW, Australia: Potential for Supergene REE Enrichment in Novel Clay-Hosted Settings

Rory Carter , Ian Graham * , David French , Indrani Mukherjee , Mathias Kapo , Karen Privat , Simon Hager , Huixin Wang , Oliver Davies

Posted Date: 21 April 2026

doi: 10.20944/preprints202604.1504.v1

Keywords: rhabdophane; churchite; secondary REE mineralization; Doradilla; skarn

 doi:10.20944/preprints202604.1504.v1

Article

Secondary Rare Earth Element (REE) Mineralization in a Skarn Regolith, Doradilla, NSW, Australia: Potential for Supergene REE Enrichment in Novel Clay-Hosted Settings

Rory Carter [1,2], Ian Graham [1,*], David French [1], Indrani Mukherjee [1], Mathias Kapo [1], Karen Privat [1,3], Simon Hager [3], Huixin Wang [4] and Oliver Davies [5]

[1] Earth and Sustainability Science Research Centre, School of Biological, Earth and Environmental Sciences, UNSW Sydney, Kensington, NSW 2052, Australia
[2] Mineral Exploration Cooperative Research Centre, School of Biological, Earth and Environmental Sciences, UNSW Sydney, Kensington, NSW 2052, Australia
[3] Electron Microscope Unit, Mark Wainwright Analytical Centre, UNSW Sydney, Kensington, NSW 2052, Australia
[4] Solid State Analysis Unit, Mark Wainright Analytical Centre, UNSW Sydney, Kensington, NSW 2052, Australia
[5] Sky Metals Pty Ltd., Orange, NSW 2800, Australia
* Correspondence: i.graham@unsw.edu.au

Abstract

With growing global REE demand, the investigation of cryptic clay-hosted rare earth element (REE) enrichment provides a better understanding of potential new prospects. This study is focused on novel REE enrichment (up to 1.38 wt.% TREO) identified in the regolith overlying the Doradilla Sn skarn prospect, northern New South Wales, Australia. The REE mode of occurrence was investigated through petrographic, field emission scanning electron microscopy (FE-SEM), micro-X-ray fluorescence (μ-XRF), and Laser Raman analyses. Secondary REE-bearing phosphate minerals are the dominant host of the REE in the regolith at Doradilla. The presence of water identified through Laser Raman confirms these minerals as rhabdophane-(La) (La(LREE,Ca)(PO_4)·$_nH_2O$), hosting most LREE, and churchite-(Y) (Y(HREE,Ca)(PO_4)·$2H_2O$), hosting most HREE. Through confirming the majority of REE being hosted in hydrated, and therefore, secondary minerals, this cryptic REE-enrichment is confirmed to be the result of secondary mineralization driven entirely by regolith-derived processes. This study highlights the importance of detailed mineral characterization in confirming the deportment of REEs in clay-hosted settings, and suggests that new protoliths (in this case a Sn skarn) have the potential to form significant, secondary REE enrichment in the overlying clay-hosted, regolith environment.

Keywords: rhabdophane; churchite; secondary REE mineralization; Doradilla; skarn

1. Introduction

The demand for critical elements such as the rare earth elements (REEs, La—Lu) has increased substantially in recent years. This is driven by REEs application in the green energy transition, their industrial and military applications, and their national supply importance [1–3]. Given this demand, there has been substantial recent attention given to well-known REE-bearing systems such as carbonatites [4–7], alkaline igneous systems [8–10], and ionic-adsorption deposits (IADs) [11–13]. While these systems receive significant focus, their geographic distribution is limited, and studies of new and potentially novel settings of REE enrichment also warrant attention. Considering this, there

 doi:10.20944/preprints202604.1504.v1

are an increasing number of geological settings for REE enrichment, with new discoveries being made at a rapid rate [14,15].

Rare earth element enrichment can be broadly separated into two groups, those driven by primary magmatic processes (e.g., carbonatites [16] and alkaline igneous systems [8,17] and those driven by secondary processes (e.g., laterites [18], IADs [12], and heavy mineral sands [19,20]). In both cases, a thorough understanding of the REE-bearing mineralogy is fundamental to understanding the processes of formation [12,17,21] as well as informing potential economic viability of the prospect via downstream extraction [22]. For REE enrichment derived from secondary processes (clay-hosted systems), understanding the REE mode of occurrence is particularly crucial, especially in novel, cryptic settings. For example, it is critical to understand if the REE are hosted in detrital monazite retained within a laterite profile [14,18], compared with secondary rhabdophane mineralization formed during weathering processes [21], or if the REE are held in their ionic state (REE^{3+}) adsorbed to clay minerals, as seen in IAD systems [12]. Each of these modes of occurrence reflects fundamentally different processes of REE enrichment in the secondary environment, and thus, determining the dominant REE form is critical to understanding a clay-hosted REE system.

While many studies have focused on supergene REE mineralization over weathered protoliths such as carbonatites [6,18] and granites [11,23], this study aims to provide a detailed description of the REE-bearing mineralogy hosted in a novel REE enriched (up to ~1.4 wt.% TREO) skarn regolith profile from the Doradilla tin system, northern NSW, Australia (Figure 1). Doradilla provides an excellent opportunity to characterize the modes of occurrence of the REEs in this previously undescribed setting. A preliminary metallurgical extraction campaign using ammonium sulphate (AS) leaching at a solution pH of 4 and 3 was not successful for economic extraction of REE [24]. This suggests that there is a negligible portion of ionically adsorbed REE within the regolith at Doradilla [24], and thus, the system can be excluded from the IAD deposit style. Therefore, the REE enrichment at Doradilla is believed to be hosted in minerals and this study has been carried out to determine the REE-bearing mineralogy.

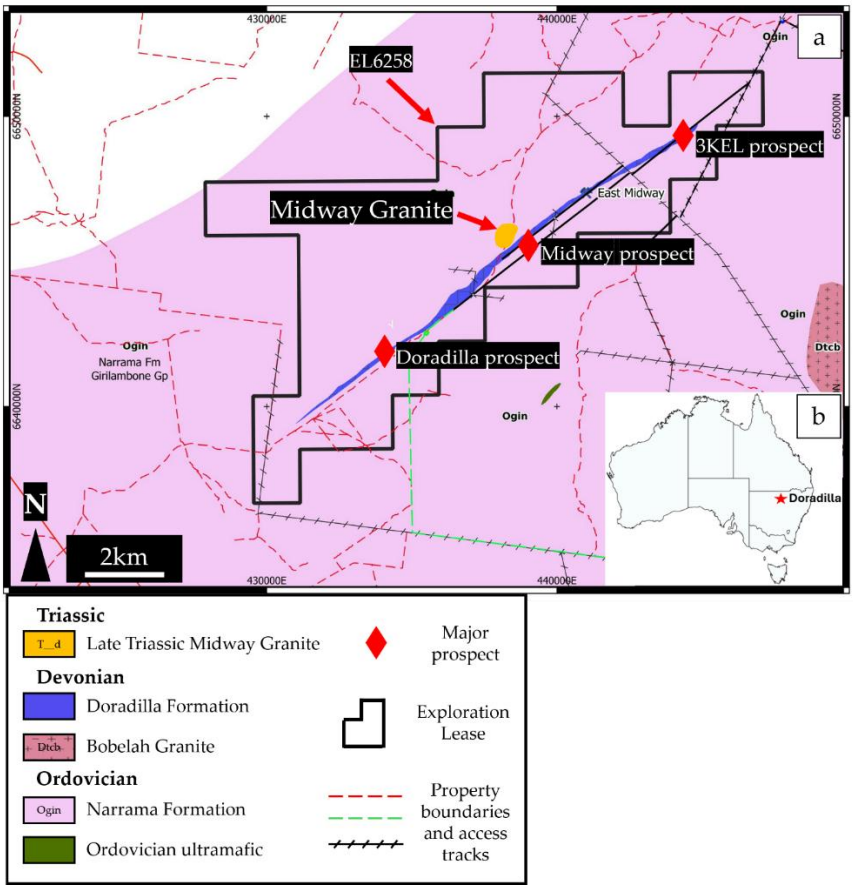

 doi:10.20944/preprints202604.1504.v1

Figure 1. Deposit geology. (**a**) Deposit geology map for the Doradilla region. Note the three major prospects situated on the Doradilla Formation (DMK line): Doradilla, Midway, and 3KEL. (**b**) Doradilla location relative to Australia.

A detailed characterization of the REE-bearing mineralogy was conducted utilizing a combination of petrography, micro-X-ray fluorescence (μ-XRF) mapping, focused ion beam scanning electron microscopy (FIB-SEM) combined with energy dispersive spectroscopy (EDS), and Laser Raman spectroscopy. Rare earth element enrichment in the regolith at Doradilla is confirmed to be due to secondary mineralization, dominated by hydrated REE-bearing phosphates, and this mineralization is largely consistent throughout the 16 km+ strike of the weathered skarn body.

2. Geological Setting

Doradilla has been the subject of intensive periods of exploration and investigation over the past 50 years with a major period of approximately 15 years of early work, beginning in the early 1970s. This work focused on the three major prospects at Doradilla (Doradilla, Midway and 3KEL), defined as the DMK line (named after the prospects) and primarily focused on tin. The DMK line is a calc-silicate unit, approximately 17 km long, trending northeast [25], ranging from 40–110 m wide, extending to at least 330 m depth, and dipping between 75° and 80° to the southeast [26–28]. Throughout the prospect, the depth of weathering extends to 100 m [27]. A thorough summary of this early period of exploration at Doradilla is provided in [29] and references therein.

Regionally, Doradilla is set within the Girilambone Group (GG), a highly deformed Ordovician turbidite succession that underlies a significant portion of Central New South Wales. In the Girilambone Zone, within which the Doradilla deposit lies, the GG consists of metasandstones, slates, phyllites, psammitic schists, pelitic schists, and quartzites, with less abundant cherts, mafic schists, and serpentinites [30].

The Doradilla prospect itself largely consists of the DMK line skarn, known formally as the Doradilla Formation [31] and the causative Midway Granite. As described by Plimer [28], the DMK line skarn is a complexly zoned, tin-rich skarn with early granoblastic grossular-rich garnet, hedenbergitic pyroxene, wollastonite and rare vesuvianite, followed by andradite-rich rims associated with quartz and Sn-bearing diopsidic pyroxene. Subsequent thin veinlets and replacements along relict bedding and cross-cutting fractures of earlier calc-silicates by calcite-malayaite is noted, followed by a final pervasive replacement of all earlier generations along relict bedding, fractures, and in discrete patches by a variable assemblage of sulfides (bornite, chalcopyrite, sphalerite, galena, arsenopyrite, pyrrhotite, and stannite), silicates (biotite, chlorite, titanite), oxides (magnetite, cassiterite), fluorite, calcite, and quartz.

The calcareous progenitor of the DMK line skarn is believed to be a limestone [32]. However, the presence of a limestone at Doradilla does not align with the known stratigraphy of the GG in the region [30]. It was therefore considered likely that a portion of the pre-skarn sequence is younger than the Ordovician GG. To test this, U-Pb dating was conducted on detrital zircons sourced from units that were distinctly laminated, but lacked the multiple deformations characteristic of the GG [33,34]. Glen et al. [9] sampled a quartz-rich metasandstone that displayed concordant ages (<5% discordance) at 417, 419 and 421 Ma. An additional sample of thinly laminated mudstone and sandstone with partial granoblastic textures, consisting of quartz with white mica, minor fine-grained xenoblastic biotite and fine-grained andalusite porphyroblasts was dated by Fraser et al. [8]. The fourteen youngest ^{206}Pb / ^{238}U ages were combined to yield a statistically coherent group with a weighted mean average of 415.9 Ma ± 3.4 Ma [33]. The ages produced from both samples strongly support the presence of an Early Devonian limestone-bearing sedimentary sequence being present in addition to the GG within the sequence at Doradilla, representing the metasiltstones and metasandstones of the Doradilla Formation. This sequence is considered to be analogous to Late Silurian-Early Devonian limestone-bearing shelf sequences of the Cobar Supergroup [35].

 doi:10.20944/preprints202604.1504.v1

The DMK line skarn formed due to the intrusion of the Midway Granite (MG). The MG outcrops to the west of the skarn line (Figure 1a) and is a volatile-rich, fractionated, and mineralized granite, with notable high Nb, Ta, Th, U, REE, Sn, and W [36]. These results led Blevin [36] to conclude that the MG is an extremely fractionated and evolved I-type granite [37], being one of the most fractionated granites identified in the Lachlan Fold Belt (LFB). The MG and a co-magmatic quartz-feldspar porphyry dyke from Doradilla were dated to the Late Triassic by Burton et al. [38]. Zircon U-Pb results produced an age of 235.1±1.4 Ma and 230.7±1.4 Ma for the MG and quartz-feldspar porphyry respectively.

Burton [32] presented a geological history of the system, representing the most current understanding: (1) deposition of deep water turbidites of the Girilambone Group during the Ordovician, (2) regional metamorphism to lower amphibolite facies and at least two generations of associated deformation during the Late Ordovician to Early Silurian Benambran Orogeny, (3) partial erosion of the Ordovician turbidite sequence followed by deposition of the limestone-bearing Cobar Supergroup equivalent rocks, at least in the Late Early Devonian, (4) Late Early Devonian deformation resulting in northeasterly trending, tight, steeply plunging, fault-bounded folds, with this deformation integrating the limestone-bearing sequence into the complex stratigraphy observed at Doradilla, and finally (5) emplacement of the Midway Granite in the Late Triassic, resulting in widespread metasomatism and development of the DMK line skarn.

The REE enrichment in the regolith at Doradilla was initially identified by SKY Metals Ltd. [39]. No previous work has been conducted on this enrichment, with this paper representing the first investigation into this aspect of the Doradilla system.

3. Samples and Methods

Rare earth element-enriched intersections were chosen from weathered profiles in each of the three prospects (3KEL in the north, Midway in the middle, and Doradilla in the south) (Figure 2). One drill hole at the 3KEL prospect (3KDD018) was selected for detailed characterization with REE enrichment occurring in heavily weathered kaolinite-rich saprolite skarn, with common secondary Fe and Ti oxides (Figure 2a–d). To conduct petrographic and electron microscopic investigations, 26 polished thin sections were produced from 3KDD018. In addition, rock chips from 30 reverse circulation drill holes were sampled, with the production of 56 polished mounts of REE-bearing regolith rock chips (Figure 2e). The polished thin sections were investigated via petrography, and both thin sections and polished mounts were investigated under scanning electron microscopy.

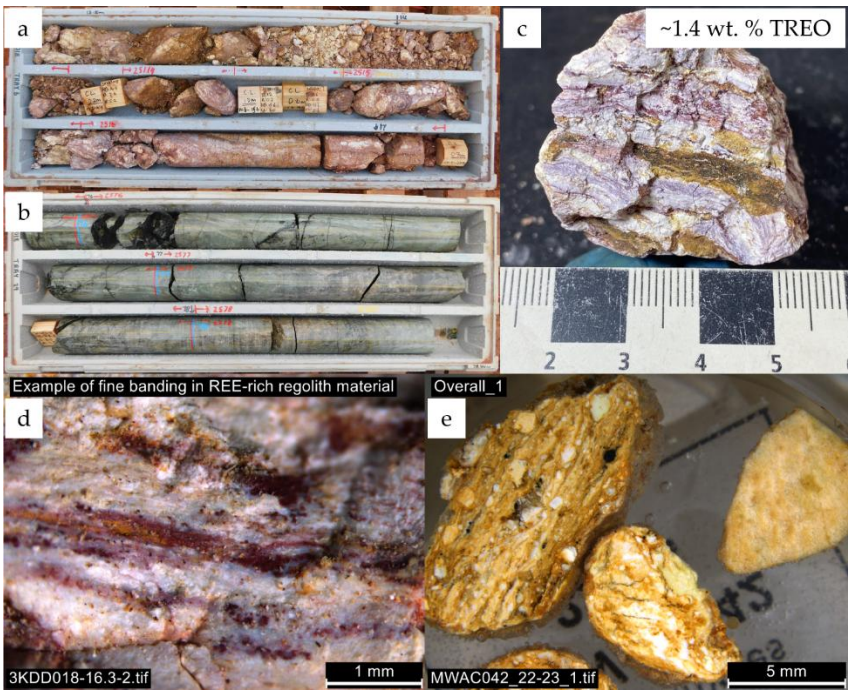

 doi:10.20944/preprints202604.1504.v1

Figure 2. Examples of samples selected for this study. (**a**) Highly weathered and (**b**) fresh skarn material photographed in drill core. (**c**) Sample photo from REE enriched regolith material (~1.4 wt. % TREO) shown in drill core photographed in (**a**). (**d**) Optical microscope imagery of sample in image (**c**) highlighting the fine-scale primary laminations of the calc-silicate are retained in this saprolized REE-rich regolith material. (**e**) Example of rock chip samples mounted in resin and polished in preparation for scanning electron microscopy investigations.

3.1. Micro-XRF Mapping

Micro X-ray fluorescence (μ-XRF) mapping was undertaken using a Bruker benchtop M4 Tornado μ-XRF at the X-ray Fluorescence Laboratory, Mark Wainwright Analytical Centre, UNSW, Sydney. The instrument is equipped with a Rh anode metal-ceramic X-ray tube. The voltage was set to 40 kV, with a current of 600 μA. X-ray spot calibration was done through digital tuning and a 20 μm spot size was employed to achieve the best spatial resolution. The fluorescent X-rays were counted with a silicon drift detector using an energy resolution ≤145 eV for MnKα. For the elemental mapping analysis, spectra were obtained every 25 μm with an acquisition time set at 100 ms/pixel. Analysis of the μ-XRF output was conducted using the Bruker M4 Tornado built-in software FP MQuant, allowing for peak identification and quantification. Critically, Nd was determined to have no interfering fluorescent peaks from other common elements, highlighted in Supplementary Material S1. Therefore, it was determined as the most suitable element to use to represent the REE distribution throughout the sample.

3.2. Scanning Electron Microscopy

Following petrographic investigation, the REE mineralization was investigated using a Zeiss Auriga Cross-Beam focused ion beam scanning electron microscope (FIB-SEM) at the Electron Microscope Unit (EMU), UNSW Sydney. This instrument is capable of high-resolution field emission (FE)SEM imagery which enabled a very detailed, sub-micron investigation of the REE mineralogy. Polished thin sections and polished resin mounts were evaporatively coated with ~20 nm of carbon prior to investigation. Mineral chemistry was investigated utilizing an Oxford Instruments X-Max 20 mm^2 energy dispersive X-ray spectroscopy (EDS) detector. An accelerating voltage of 15-20 kV was employed, with 20 kV being favored as it enabled the identification of the Y Kα peak at ~15 kV.

In addition, a ThermoFisher Scientific Verios field emission scanning electron microscope (FE-SEM) coupled with an Oxford Instruments Unity BEX detector at the UNSW Sydney EMU was utilized to investigate zonation in the chemistry of the REE minerals. The EDS data were processed using Oxford Aztec 6.3 software. EDS elemental maps were background subtracted and peak deconvolution was applied to obtain more reliable elemental distributions.

3.3. Laser Raman

Laser Raman analysis was conducted on representative REE-bearing phosphate minerals to confirm the presence of water in the mineral structure, thus defining rhabdophane and churchite, rather than monazite or xenotime. The presence of water typically produces a strong, broad OH^- band in the Raman spectrum between 3200 cm^{-1} and 3600 cm^{-1} [40]. Phase effects in solid materials often result in this band being narrower [41]. Raman spectra were obtained via an inVia Reflex Raman Microscope at the Spectroscopy Laboratory, UNSW Sydney. An excitation wavelength of 532 nm with a 100x objective was utilized. Integration times for a single spectrum were between 10-20 s and averaged from 1 to 3 accumulations. The characteristic spectra of the REE minerals were obtained using 50% laser power, 10 s working time, and a 3 composite spectra. This analysis was conducted on carbon coated polished mounts.

 doi:10.20944/preprints202604.1504.v1

4. Results

4.1. Petrography and Micro-XRF Mapping

Petrographic investigations were coupled with micro-XRF mapping to locate the REE-bearing species in the mineralized intersections. Petrography revealed that there were two major regolith zones within which REE mineralization was hosted: (1) entirely kaolinized saprolite (Figure 3a) comprised predominantly of kaolinite with a very common iron oxide overprint, common quartz and uncommon detrital zircon and (2) laminated calc-silicate saprock, dominated by zones richer in Fe-bearing smectite (Figure 3b) and remnant K-feldspar-quartz rich weathered metasediment (Figure 3c,d), with more subordinate kaolinite, quartz, an array of secondary iron, titanium and manganese oxides, and detrital zircon. With increasing depth in the weathered profile, remnant garnet becomes more common (Figure 3e).

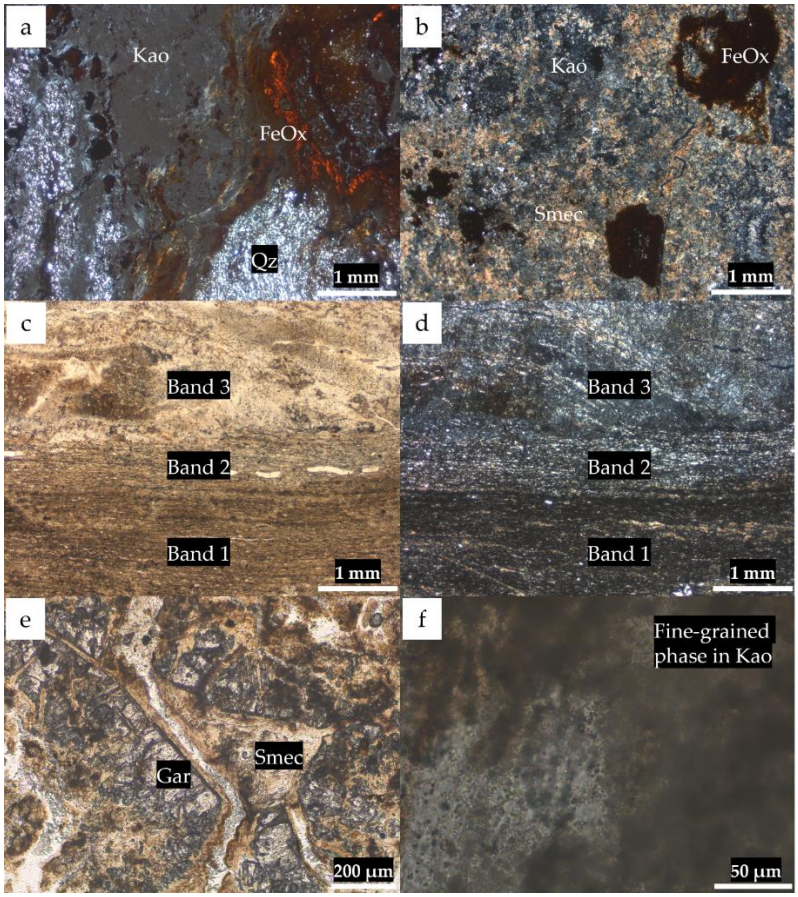

Figure 3. Photomicrographs of weathered Doradilla Formation skarn. (**a**) Example of entirely kaolinized saprolite material, with retention of quartz-rich patches, and common secondary Fe oxide infill (UXP). (**b**) Example of smectite-dominant regolith zones with more subordinate kaolinite-quartz fill and patchy Fe oxide (UXP). PPL (**c**) and UXP (**d**) example of the fine-scale bedding identified within the weathered calc-silicate-overprinted laminations from the Doradilla Formation. (**e**) Partially weathered garnet skarn saprock, with remnant skeletal garnet set in a smectite-rich groundmass (PPL). (**f**) Evidence of very fine-grained phases in kaolinite groundmass as highlighted by Nd clustering in Figure 4b (PPL). Note, UXP = image taken under crossed polars and PPL = plain polarized light image. Note: Kao = kaolinite, FeOx = iron oxides, Qz = quartz, Smec = smectite, Gar = garnet.

Critically, the utilization of micro-XRF (µ-XRF) mapping of the polished thin sections (Figure 4a) allowed for the identification of particularly REE-rich zones in the samples. These were otherwise highly cryptic in hand specimen (Figure 2c,d). Figure 4b illustrates the distribution of Al, Fe, Ti, and

 doi:10.20944/preprints202604.1504.v1

Nd throughout the entirely kaolinized saprolite that contains up to 1.4 wt. % TREO. This figure highlights the effectiveness of mapping Nd distribution throughout the highly weathered samples. Neodymium occurs in localized clusters and is noted to be particularly concentrated within certain bands of the relict laminations that were observed pervasively throughout the fresh DMK line calc-silicate. These results were supported by petrographic investigations revealing opaque clusters of exceptionally fine-grained minerals (Figure 3f). These were thought to be the likely REE-bearing phases, however, finer-scale investigations were deemed necessary for accurate characterization.

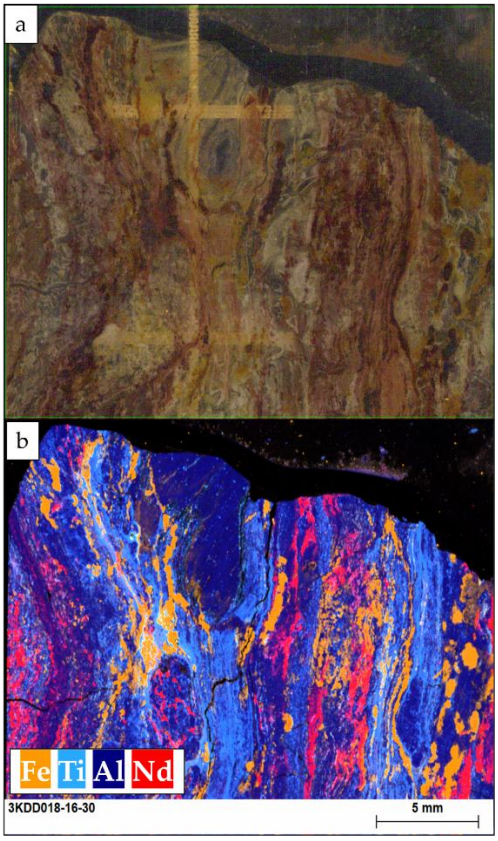

Figure 4. Micro-X-ray Fluorescence (XRF) map of polished thin section from REE-rich regolith material in Figure 2c. (**a**) Image of the polished thin section mapping area. (**b**) Micro-XRF map highlighting the distribution of Fe (orange), Ti (light blue), Al (dark blue), and Nd (red) throughout the surface of the polished thin section. Note the clustering of the red Nd to particular remnant beds of the protolith.

4.2. REE Mineralogy

4.2.1. Rhabdophane

Field emission-scanning electron microscopy (FE-SEM) enabled the characterization of the previously identified potential REE-bearing mineral clusters. This work showed that these minerals are rhabdophane, commonly observed in clusters of individual grains that are approximately 200 nm–2 μm in size (Figure 5a). These individual mineral grains occur in a range of textures, commonly noted as needle-like clusters and blocky laths (Figure 5b). Uncommonly, rhabdophane clusters were observed infilling pore space of partially weathered primary minerals, particularly K-feldspars. In one sample, detrital monazite from the Devonian metasedimentary unit is interpreted to have been largely replaced by rhabdophane. Where more space was available for mineral growth, the rhabdophane occurs as well-developed, subhedral to euhedral coarser clusters up to ~150 μm in length (Figures 5c).

Figure 5g presents a characteristic EDS spectrum for the phase identified as rhabdophane. Lanthanum and Nd are the dominant LREE and Ce is markedly depleted. A minor Ca peak is always

 doi:10.20944/preprints202604.1504.v1

present and, less commonly, S. The EDS results do not provide any strong evidence for the presence of Th. Overall, the EDS results suggest that this is a rhabdophane-(La) ($La(LREE,Ca)(PO_4)\cdot_nH_2O$). This chemistry is observed in both the fine-grained clusters and the more well-developed, coarser grains, supporting the conclusion that they are the same phase.

Back scattered electron (BSE) imagery revealed complex zonation within the larger clusters of rhabdophane. Figure 6a–f presents a map of selected elements throughout one such zoned grain. It can be seen that La is the most dominant cation, with a more subordinate Nd enriched rim. These larger grains appear to be amalgamations of smaller subhedral crystals. A La (LREE)-depleted core is observed for these smaller grains, with a subsequent more LREE-enriched rim. The outer Nd-rich rim possibly indicates two periods of mineral growth, with amalgamation of the La-rich subhedral grains, followed by a final rim incorporating more Nd. Figure 6e indicates the presence, but relative to the LREE, lower intensity, of Y in this rhabdophane grain, highlighting its ability to take some of the smaller HREE ions into its structure.

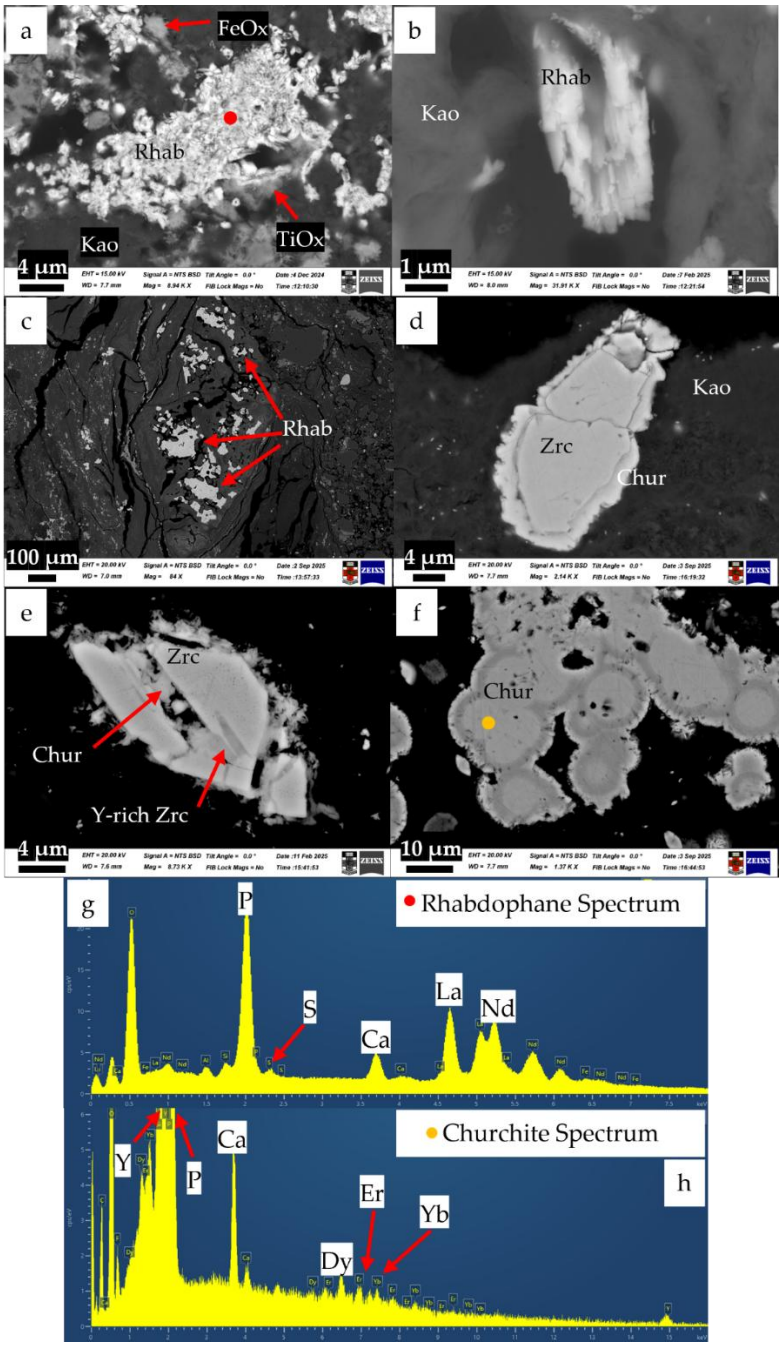

 doi:10.20944/preprints202604.1504.v1

Figure 5. Summary of scanning electron microscopic investigation of the primary REE minerals at Doradilla. (**a**) Characteristic clusters of fine-grained (200 nm–2 μm) individual rhabdophane grains, co-occurring with secondary Fe and Ti oxides infilling in kaolinized saprolite. (**b**) Example of fine-grained blocky laths of rhabdophane. (**c**) Coarser clusters of rhabdophane up to ~150 μm in size. (**d**) Common occurrence of churchite rim on detrital zircon grains. (**e**) Mechanical damaged and metamictized zircon grain with darker, Y-rich patches, and rims of fine-grained churchite. (**f**) Zoned, colloidal clusters of churchite, occurring up to 100-150 μm. (**g**) Characteristic EDS spectrum of rhabdophane, taken from location shown by red dot in (**a**). Note the marked lack of Ce, which if present would produce a major (Lα1) peak at 4.84 keV between the major La and Nd Lα1 peaks. (**h**) Characteristic EDS spectrum of churchite, taken from location shown by orange dot in (**f**). Note: Rhab = rhabdophane, Kao = kaolinite, TiOx = titanium oxides, FeOx = iron oxides, Zrc = zircon, Chur = churchite.

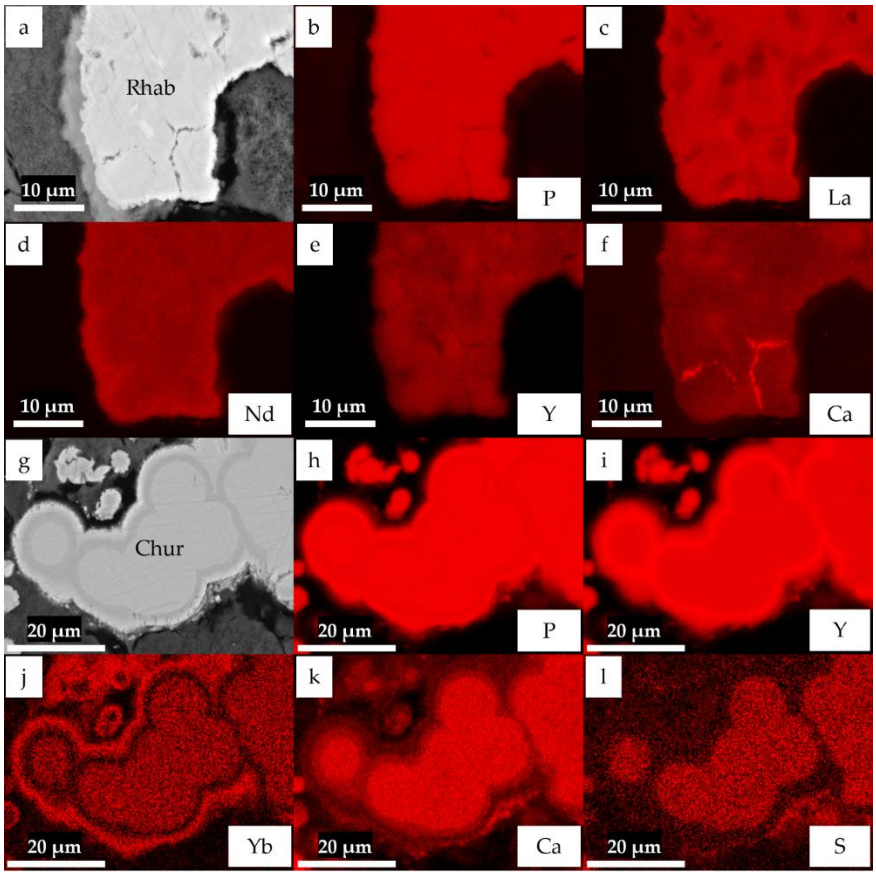

Figure 6. EDS maps of the rhabdophane grain and churchite cluster shown in the BSE images in (**a**) and (**g**) respectively. (**b**–**f**) Maps of the P (**b**), La (**c**), Nd (**d**), Y (**e**) and Ca (**f**) distribution through the rhabdophane grain in (**a**). (**h**–**l**) Maps of the P (**h**), Y (**i**), Yb (**j**), Ca (**k**) and S (**l**) distribution through the churchite cluster in (**g**).

4.2.2. Churchite

The only HREE-rich mineral identified in the regolith at Doradilla was churchite. It is frequently observed as a fine-grained rim (<1 μm–5 μm) on detrital zircon grains (sourced from the Devonian metasedimentary unit) in the weathering profile of the DMK line skarn (Figure 5d). In regions of high REE enrichment within the regolith profile, this HREE phosphate rim on zircon is very common. However, in unmineralized regolith horizons, detrital zircons do not display this churchite rim. The zircon grains with this rim commonly display signs of significant mechanical degradation and metamictization (Figure 5e). Similar to the rhabdophane, the churchite was also noted to rarely occur as coarser clusters. These comprised individual colloidal grains, commonly 10-15 μm, combining up to ~150 μm in size in a small number of samples investigated (Figure 5f).

 doi:10.20944/preprints202604.1504.v1

A characteristic EDS spectrum of the churchite identified is presented in Figure 5h. This highlights that Y is the dominant cation in this mineral, present as a left-hand shoulder on the P peak. The presence of a peak at 15 kV corresponds to the Y Kα peak and confirms its presence. More subordinate HREE peaks are also evident in the spectrum. As in the LREE phosphate, minor Ca and trace S are also present. The EDS results suggest that this phase is a churchite-(Y) ($Y(HREE,Ca)(PO_4)\cdot 2H_2O$).

The EDS map of these colloids in Figure 6g–l reveals a clear sequence of varying chemical composition as the colloidal growth progressed. The mid-grey core in the BSE image corresponds to the greatest intensity of Ca, co-located with minor S present in the mineral. This is surrounded by a thinner, darker middle rim which appears to be most abundant in Y relative to the other zones, being noticeably depleted in other HREE (represented by Yb), and showing a relative reduction in P. Finally, the outermost, brightest rim is clearly enriched in HREE, as evidenced by the Yb map, with a reduction in Y, an increase in P, low levels of Ca, and no significant S.

4.2.3. Cerianite

Cerianite is a common mineral in the regolith at Doradilla. The cerianite was observed to be particularly concentrated in zones and bands in Mn oxide-rich veinlets and alteration patches (Figure 7a). Individual cerianite grains appear to be < 1 micron in size (Figure 7b). The EDS spectra in Figure 7e highlights the composition of the cerianite zone shown in Figure 5g. Minor P, Pb, and Ca are noted (Figure 7e), however, it is difficult to conclude if these elements are inclusions in the cerianite, or fine-grained intergrowths of co-occurring phases, with exceptionally fine-grained relationships commonly observed throughout these REE-bearing assemblages. The intimate association with Mn oxides is noted frequently in the REE mineralized zones of the Doradilla regolith profile. This Mn concentration appears to be localized to relict calc-silicate rich zones of the profile, with Mn most likely sourced from the primary skarn minerals such as clinopyroxene.

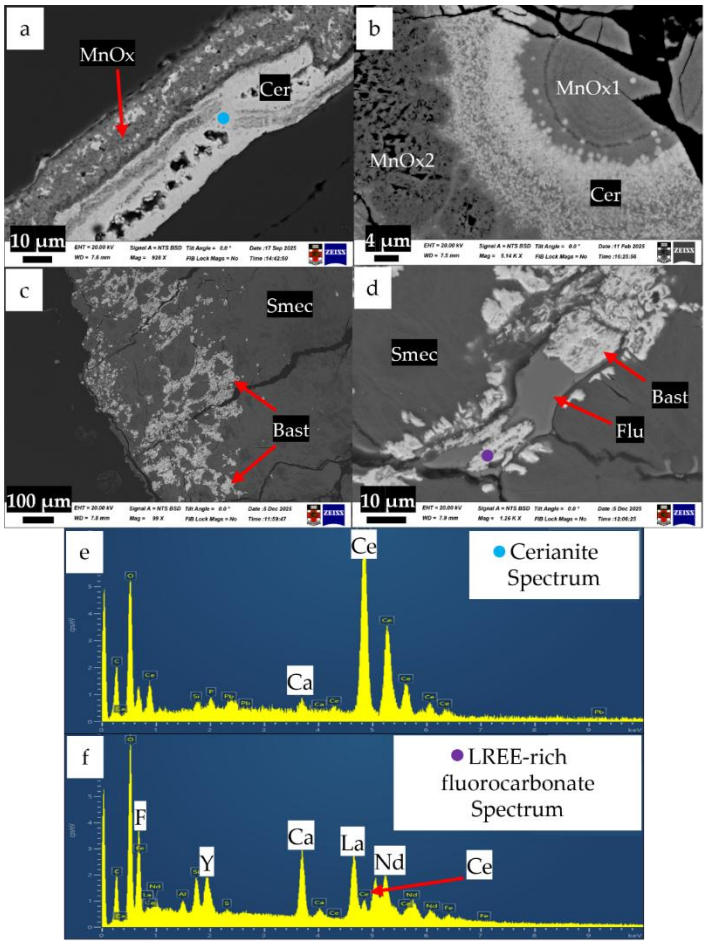

 doi:10.20944/preprints202604.1504.v1

Figure 7. Summary of scanning electron microscopic investigation of the secondary REE minerals at Doradilla. (**a**) Mn oxide vein with cerianite-rich band. (**b**) Intimate association of Mn oxides and cerianite. (**c**) Abundant patch of LREE-rich fluorocarbonates in smectite / fluorite partially weathered saprock skarn. (**d**) Direct replacement of fluorite by LREE-rich fluorocarbonate (here noted as Bastnäsite). (**e**) Characteristic EDS spectrum of cerianite, taken from location shown by blue dot in (**a**). (**f**) Characteristic EDS spectrum of LREE-rich fluorocarbonate, taken from location shown by purple dot in (**d**). Note: MnOx = manganese oxides, Cer = cerianite, Flu = fluorite, Bast = bastnäsite (representing LREE-rich fluorocarbonate).

4.2.4. Fluorocarbonates

Rare earth element-bearing fluorocarbonates were identified to be locally significant in a small number of samples from the Midway and Doradilla prospects (Figure 5c). Two drill holes (MWAC052 / 053) from the north of the Midway prospect contained particularly significant REE fluorocarbonate mineralization in partially weathered saprock skarn chips. Figure 5d and the corresponding EDS spectra in Figure 5f suggests that these minerals are a LREE-rich fluorocarbonate with a La dominance, while also containing appreciable Nd, Y, and Ca, with a more subordinate Ce concentration. Texturally, these fluorocarbonates are particularly concentrated within remnant, fluorite-rich, partially weathered saprock skarn. This suggests these phases are alteration products of the fluorite and therefore, secondary, and interestingly, no REE-bearing phosphate phases were identified to locally co-occur. The Ca peak identified in this phase is the most significant out of all the REE identified during the investigation. The fine-grained nature of these phases prevents accurate quantification through SEM-based analytical techniques, however, based on the EDS data this phase is considered most likely to be a secondary parisite-(La) ($CaLa_2(CO_3)_3F$), with the caveat that, Ca substitution is possible in both hydroxylbastnäsite-(La) ($La(LREE,Ca,Y)(CO_3)(OH,F)$ or the anhydrous bastnäsite-(La) $La(LREE,Ca,Y)(CO_3)F$. Considering these uncertainties, these phases are referred to as LREE-rich fluorocarbonates hereafter. While these LREE-rich fluorocarbonates are locally significant, the REE-bearing phosphates are substantially more abundant throughout the skarn regolith at Doradilla.

4.3. Laser Raman Spectroscopy

Laser Raman spectroscopy was used to investigate the presence of water in the larger clusters of both LREE- and HREE-rich phosphate species. The grain size of the larger clusters of both phases (Figure 5c,f) (> 20 micron) enabled a reliable investigation of these discrete phases using Raman techniques. The LREE-bearing phase presented typical vibrational modes associated with PO_4 [42]. This includes a dominant v_1 stretching (988 cm^{-1}), moderate v_2 bending (470 cm^{-1}) and v_3 (1096 cm^{-1}) peaks, and a minor peak associated with the v_4 bending mode (634 cm^{-1}) (Figure 8). Similarly, the HREE-bearing phase also presented typical PO_4 vibrational modes for v_1 (996 cm^{-1}), v_2 (478 cm^{-1}), v_3 (1058 cm^{-1}), and v_4 (660 cm^{-1}) (Figure 8). The Raman spectra of a monazite grain from a sample of the Midway Granite is presented for comparison in Figure 8. In the 3000–3600 cm^{-1} region both the LREE- and HREE-rich phases contain multiple peaks compared with the barren monazite spectra. Figure 8b highlights that the LREE-rich phase has a broader region with peaks at 3138 cm^{-1} and 3200 cm^{-1}, as well as a larger peak at 3479 cm^{-1}. Similarly, there is a broader peak at 3263 cm^{-1} and smaller, more discrete peaks at 3417 cm^{-1}, 3466 cm^{-1}, and 3506 cm^{-1} for the HREE-rich phase. These peak regions are characteristic of stretching vibrations in H_2O [43–45]. These results highlight the presence of water in the phosphate minerals that dominate the regolith at Doradilla, thus confirming that these minerals are rhabdophane and churchite, and of secondary origin.

Several peaks between 1200 and 2800 cm^{-1} in the Raman spectra were also observed. However, these are believed to be the result of fluorescence artefacts and due to the carbon coating on the polished mounts. As highlighted previously, these regions are not relevant to the identification of characteristic PO_4 bonds (~300–1200 cm^{-1}) or H_2O bonds (~ 3200–3500 cm^{-1}) that were the focus of this study and as such, these spectral features are not included in our analysis.

 doi:10.20944/preprints202604.1504.v1

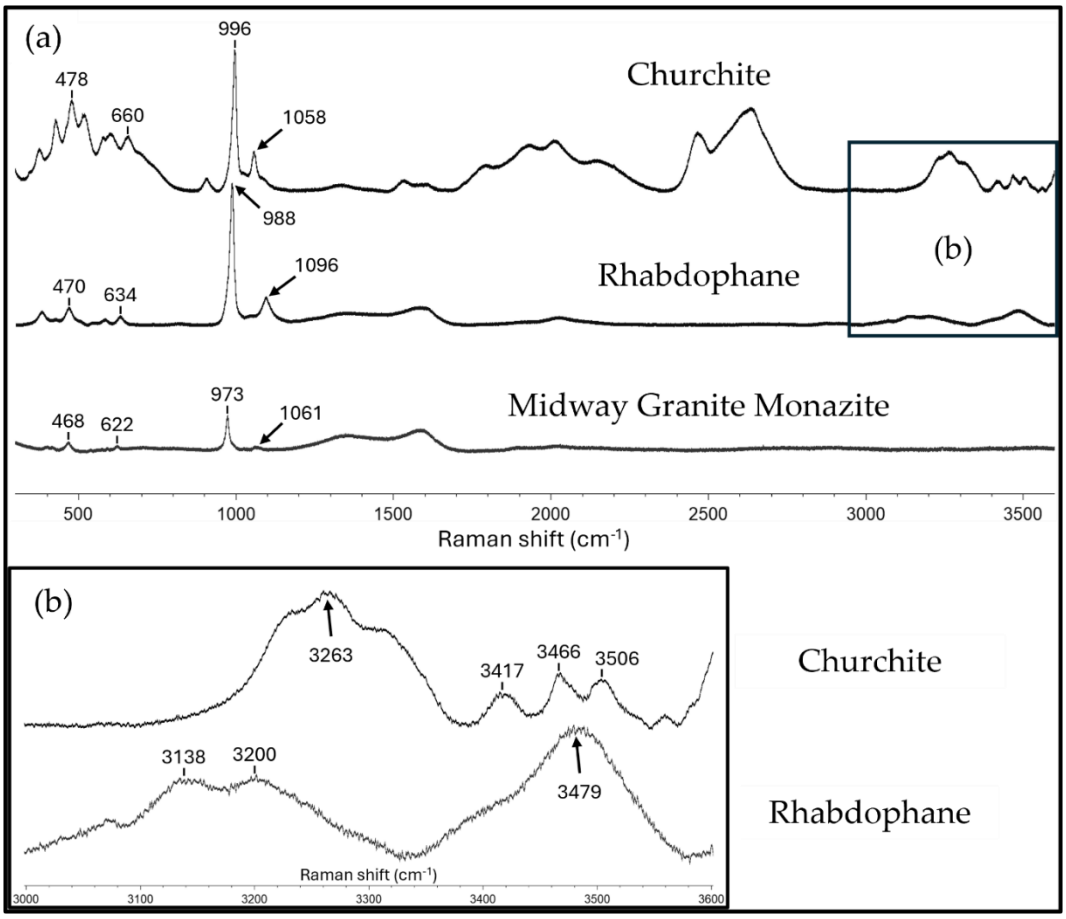

Figure 8. Laser Raman spectra for churchite and rhabdophane from Doradilla, compared with monazite from the Midway Granite. (**a**) Overall spectrum for churchite, rhabdophane and monazite from 300–3600 cm^{-1} in the Raman shift. (**b**) Inset on 3000–3600 cm^{-1} in the Raman shift for the churchite and rhabdophane, clearly highlighting the presence of peaks in this region which are considered to represent stretching of the O-H bond in H_2O present in these minerals.

5. Discussion

5.1. REE Mineralization at Doradilla

The results presented confirm that the REE mineralogy in the skarn regolith is dominated by rhabdophane-(La) with a proposed formula of (La(LREE,Ca)$(PO_4)\cdot_nH_2O$) and churchite-(Y) with a proposed formula of (Y(HREE,Ca)$(PO_4)\cdot 2H_2O$). Common cerianite and rare, localized LREE-rich fluorocarbonates were also observed hosted within the variably weathered (entirely saprolized to partially weathered saprock) DMK line skarn. Textural evidence (e.g., fine-grained clusters associated with secondary oxide species infilling clays) in combination with EDS spectra proved effective at characterizing these minerals. These results strongly suggest that this mineralization is secondary in nature, having formed as low-temperature, regolith-derived products.

However, identifying the presence of water in the rhabdophane and churchite is crucial. The similarities between monazite (LREE(PO_4)) and rhabdophane (LREE$(PO_4)\cdot_nH_2O$), and likewise, those similarities between xenotime (HREE(PO_4)) and churchite (HREE$(PO_4)\cdot 2H_2O$) mean that conclusive separation of these minerals is impossible without confirming the presence of water in the mineral structure [21,45]. Studies have shown that identifying the presence of water through Laser Raman spectroscopy is an effective tool to differentiate between anhydrous and hydrated REE-bearing phosphates [43,45]. These results were replicated here, successfully identifying the presence of water in both the LREE- and HREE-rich phosphates in the regolith at Doradilla, while also effectively comparing these with anhydrous monazite from the Midway Granite (Figure 8). As a result, the

 doi:10.20944/preprints202604.1504.v1

implications of the textural and chemical results are reaffirmed, allowing for a confident conclusion that this novel setting of REE enrichment was formed during weathering of the protolith skarn. The implications of this are discussed further below.

The consistent presence of Ca in both rhabdophane (Figure 5g and churchite (Figure 5f) suggests that the REE-bearing mineralizing fluids contained appreciable Ca and that substitution is occurring. A complete solid-solution exists between cheralite-monazite, and substitution of Ca for REE^{3+} into monazite group species (of which rhabdophane is a member) is well-documented [46]. The presence of S in addition to Ca may indicate that a coupled substitution mechanism was operating. Sulfur-bearing monazite [47] and rhabdophane [45] have been previously identified and coupled substitution mechanisms have been suggested as a process for the incorporation of both S and Ca, for example: $S^{6+} + Ca^{2+} \leftrightarrow REE^{3+} + P^{5+}$ [48]. While EDS is not quantitative, the Ca peak is substantially stronger in the LREE-rich fluorocarbonates (Figure 7f) compared with the rhabdophane (Figure 5g). This greater enrichment may point to the formation of parisite, rather than a bastnäsite with Ca-substitution where LREE-rich fluorocarbonates are locally developed at Doradilla. This may be explained by the intimate relationship with fluorite, with direct replacement of the fluorite by the LREE-rich fluorocarbonate commonly observed (Figure 7d). Finally, the BSE maps in Figure 6 point to a relatively Ca-rich and S-bearing fluid during early mineral growth of the REE-bearing phosphates, particularly highlighted by the churchite in Figure 6k,l. These maps suggest a relative increase in REE concentration as the minerals grew, with a final stronger rim of REE concentration seen for La (Figure 6c) and Nd (Figure 6d) in the rhabdophane and particularly noted for Yb (Figure 6j—considered a proxy for all the HREE) in the churchite.

The intimate association of churchite with detrital zircon grains can be explained by their shared crystal structure. Xenotime group minerals (which includes churchite) have a zircon-type structure, and a structural relationship exists between xenotime and zircon [49]. This association suggests that the zircon likely provided a favorable nucleation site for the churchite rim. Furthermore, metamictization-induced crystal structure damage of the zircon (as evidenced by fractures and abundant spherical pores in the zircon in Figure 5e) may also have enabled the liberation of HREE from the zircon [50], allowing for subsequent precipitation of churchite in the presence of a P-rich fluid. Furthermore, EDS results suggested the presence of Y-rich patches within zircon grains (Figure 5e), potentially representing an intermediate churchite-zircon phase, with xenotime-zircon intermediaries having been previously identified [51].

5.2. Presence of Cerianite and Paragenetic Implications

The mineralogical investigations of this study suggest that there is an intimate relationship between cerianite (CeO_2) and Mn oxides in the regolith at Doradilla. Cerianite is localized to regions of the weathered profile that have abundant Mn oxides (Figure 5g,h). Studies of Ce partitioning in marine environments have shown that aqueous Ce^{3+} would be partially oxidized to Ce^{4+} when complexed by Fe-Mn (oxydr)oxides [52]. Furthermore, Mn oxides are known to have an intimate association with Ce in marine systems, with high Ce concentrations and distinct positive anomalies [53]. In highly oxidizing environments, such as REE-enriched regolith profiles in IAD systems, it is common to see a consistent positive Ce anomaly overlying REE-enriched horizons, interpreted to be directly controlled by highly oxidizing conditions [12]. However, in Mn oxide-rich regolith profiles, such as at Doradilla, it is likely that the Mn oxides will very efficiently sequester the aqueous Ce^{3+} through complexation and oxidation to Ce^{4+}, forming cerianite, and localizing its distribution. As a result, there is not an obvious overlying Ce-rich horizon that vectors towards the highly REE-enriched mineralization below. This poor constraint on Ce anomalies in Australian clay-hosted REE prospects has been noted by Knorsch et al. [54], with further work needed to constrain the relationships between cerianite and co-occurring Ce-depleted, REE-enriched, secondary minerals.

This relationship can also help to explain the significant Ce-depletion observed in a portion of the rhabdophane at Doradilla (Figure 5g). The formation of cerianite prior to rhabdophane would

 doi:10.20944/preprints202604.1504.v1

result in a Ce-depleted REE-bearing fluid that subsequently formed the rhabdophane observed in this study.

5.3. Skarn Regolith Settings as a Host for REE Mineralization

The Doradilla skarn is believed to be a novel setting for clay-hosted REE mineralization. While similar REE enrichment in weathered profiles overlying granite [12], carbonatite [18], and other [14,15] protoliths have garnered significant attention, the REE mineralogy of a skarn-hosted regolith setting has not previously been described. As no previous work has been conducted, the aim of this study was to accurately characterize the REE mineralization at Doradilla. This is critical because in some clay-hosted REE mineralization settings, detrital resistate phases (including monazite and xenotime) are the dominant REE mode of occurrence, for example heavy mineral sands [19,20] and laterite profiles [18].

Through accurately characterizing the dominant REE mineralization as hydrated REE-bearing phosphates, a transported, detrital and/or residual model for REE enrichment at Doradilla can be confidently discounted. The mineralogy of these systems would be dominated by anhydrous REE-bearing phosphates (monazite / xenotime). Furthermore, rhabdophane and churchite are only known to form in low temperature (commonly ambient [14,21,44] and rarely up to < 200 °C) environments [45], thus supporting secondary mineralization in the regolith. In addition, the skarn protolith setting suggests any skarn-derived REE-bearing phosphates would have formed at temperatures significantly above 200 °C. Finally, the common intimate intergrowths (Figure 5a) of the REE-bearing phosphates with other co-occurring regolith-derived minerals such as anatase and Fe oxides provide further support for secondary mineralization, and confirmation against the residual model. As a result, the findings presented here strongly support that the novel mineralization in this skarn regolith setting is secondary in nature, formed through intense and pervasive in-situ weathering of the DMK line skarn package, with subsequent supergene REE enrichment.

5. Conclusions

This study investigated the significant REE enrichment hosted in the novel skarn regolith setting at Doradilla. The results show that the REE mineralization is dominated by secondary, hydrated REE-bearing phosphates. The LREE are hosted in a rhabdophane-(La) ($La(LREE,Ca)(PO_4)\cdot_nH_2O$), commonly occurring as individual fine-grained (1-2 μm) grains in larger clusters. The HREE are hosted in a churchite-(Y) ($Y(HREE,Ca)(PO_4)\cdot 2H_2O$), displaying intimate associations with detrital zircon, occurring very commonly as a thin rim on those zircon grains in REE mineralized horizons. Both rhabdophane and churchite are noted to rarely develop into euhedral grains in clusters up to 150 μm in size. Cerianite is commonly observed throughout the regolith profile above the skarn, and Mn-bearing protoliths are proposed to control the distribution of cerianite at Doradilla.

The presence of water was successfully identified in both rhabdophane and churchite, confirming that these minerals are hydrated REE-bearing phosphates. The consistency of this mineralization throughout the 16km+ strike of the weathered skarn body and the identification of its hydrated state supports the conclusion that this novel clay-hosted REE mineralization at Doradilla is secondary in nature, formed entirely during development of the regolith profile. Furthermore, these results highlight the economic potential of novel protoliths, in this case the DMK line skarn, to serve as suitable precursors to supergene REE mineralization. Future work is currently underway to investigate the formational mechanisms of this novel REE mineralization, driven by this key conclusion that it is secondary in nature.

Supplementary Materials: The following supporting information can be downloaded at the website of this paper posted on Preprints.org

Author Contributions: Conceptualization, R.C., I.G., D.F., O.D.; methodology, R.C., I.G., K.P., S.H., H.W.; software, R.C.; validation, R.C.; formal analysis, R.C.; investigation, R.C., M.K.; resources, I.G., O.D.; data

 doi:10.20944/preprints202604.1504.v1

curation, R.C.; writing—original draft preparation, R.C.; writing—review and editing, R.C., I.G., D.F., I.M.; visualization, R.C.; supervision, I.G.; project administration, I.G.; funding acquisition, I.G. All authors have read and agreed to the published version of the manuscript.

Funding: This research was funded by the Mineral Exploration Cooperative Research Centre (MinEx CRC). Financial support was also provided by SKY Metals Limited. RC was supported by the Commonwealth through an Australian Government Research Training Program Scholarship. Further details are provided in Acknowledgments.

Data Availability Statement: Data will be made available upon request.

Acknowledgments: This work has been supported by the Mineral Exploration Cooperative Research Centre whose activities are funded by the Australian Government's Cooperative Research Centre Program. This is MinEx CRC Document 20**/****. This project has received financial support from SKY Metals Limited and we thank the staff at SKY Metals for providing access to drill core and their warm hospitality and technical insights during visits to their facilities. The authors acknowledge the following facilities housed within the Mark Wainwright Analytical Centre (MWAC) at UNSW Sydney: the scientific and technical assistance of B. Ghinangju and B. David at the Spectroscopy Laboratory, the staff from the X-ray Fluorescence (XRF) lab, X-ray Facility, and of Microscopy Australia at the Electron Microscope Unit (EMU). We would also like to thank Adelaide Petrographics and Mira van dey Lay for producing excellent polished thin sections and blocks of such difficult samples. RC was supported by the Commonwealth through an Australian Government Research Training Program Scholarship [DOI: https://doi.org/10.82133/C42F-K220].

Conflicts of Interest: The authors declare no conflicts of interest.

References

1. Goodenough, K.M.; Wall, F.; Merriman, D. The Rare Earth Elements: Demand, Global Resources, and Challenges for Resourcing Future Generations. *Natural Resources Research* **2018**, *27*, 201-216, doi:10.1007/s11053-017-9336-5.
2. Balaram, V. Rare earth elements: A review of applications, occurrence, exploration, analysis, recycling, and environmental impact. *Geoscience Frontiers* **2019**, *10*, 1285-1303, doi:10.1016/j.gsf.2018.12.005.
3. Chen, P.; Ilton, E.S.; Wang, Z.; Rosso, K.M.; Zhang, X. Global rare earth element resources: A concise review. *Applied Geochemistry* **2024**, *175*, 106158, doi:https://doi.org/10.1016/j.apgeochem.2024.106158.
4. Andersen, A.K.; Clark, J.G.; Larson, P.B.; Donovan, J.J. REE fractionation, mineral speciation, and supergene enrichment of the Bear Lodge carbonatites, Wyoming, USA. *Ore Geology Reviews* **2017**, *89*, 780-807, doi:https://doi.org/10.1016/j.oregeorev.2017.06.025.
5. Anenburg, M.; Mavrogenes, J.A.; Frigo, C.; Wall, F. Rare earth element mobility in and around carbonatites controlled by sodium, potassium, and silica. *Science Advances* **2020**, *6*, eabb6570, doi:10.1126/sciadv.abb6570.
6. Zhukova, I.A.; Stepanov, A.S.; Jiang, S.-Y.; Murphy, D.; Mavrogenes, J.; Allen, C.; Chen, W.; Bottrill, R. Complex REE systematics of carbonatites and weathering products from uniquely rich Mount Weld REE deposit, Western Australia. *Ore Geology Reviews* **2021**, *139*, 104539.
7. Li, X.-C.; Fan, H.-R.; Su, J.-H.; Groves, D.I.; Yang, K.-F.; Zhao, X.-F. Giant Rare Earth Element Accumulation Related to Voluminous, Highly Evolved Carbonatite: A Microanalytical Study of Carbonate Minerals From the Bayan Obo Deposit, China. *Economic Geology* **2024**, *119*, 373-393, doi:10.5382/econgeo.5060.
8. Dostal, J. Rare Earth Element Deposits of Alkaline Igneous Rocks. *Resources* **2017**, *6*, doi:10.3390/resources6030034.
9. Beard, C.D.; Goodenough, K.M.; Borst, A.M.; Wall, F.; Siegfried, P.R.; Deady, E.A.; Pohl, C.; Hutchison, W.; Finch, A.A.; Walter, B.F.; et al. Alkaline-Silicate REE-HFSE Systems. *Economic Geology* **2023**, *118*, 177-208, doi:10.5382/econgeo.4956.
10. Wang, M.; Hei Li, M.Y.; Zhou, M.-F.; Zhou, J.-X.; Sun, G.; Zhou, Y.; Li, Y. Enrichment of Rare Earth Elements During the Weathering of Alkaline Igneous Systems: Insights from the Puxiong Regolith-Hosted Rare Earth Element Deposit, SW China. *Economic Geology* **2024**, *119*, 161-187, doi:10.5382/econgeo.5024.

 doi:10.20944/preprints202604.1504.v1

11. Sanematsu, K.; Watanabe, Y. Characteristics and Genesis of Ion Adsorption-Type Rare Earth Element Deposits. *Rare Earth and Critical Elements in Ore Deposits* **2016**, *18*, 0, doi:10.5382/Rev.18.03.
12. Li, M.Y.H.; Zhou, M.-F.; Williams-Jones, A.E. The Genesis of Regolith-Hosted Heavy Rare Earth Element Deposits: Insights from the World-Class Zudong Deposit in Jiangxi Province, South China. *Economic Geology* **2019**, *114*, 541-568, doi:10.5382/econgeo.4642.
13. Borst, A.M.; Smith, M.P.; Finch, A.A.; Estrade, G.; Villanova-de-Benavent, C.; Nason, P.; Marquis, E.; Horsburgh, N.J.; Goodenough, K.M.; Xu, C.; et al. Adsorption of rare earth elements in regolith-hosted clay deposits. *Nat Commun* **2020**, *11*, 4386, doi:10.1038/s41467-020-17801-5.
14. Knorsch, M.; Gazley, M.; Ince, M.; Kartal, M.; Trunfull, E.; Lilly, K.; Piechocka, A.; Lu, Y.; Cooke, B.; Kelaart, C. Characterisation of clay-hosted rare-earth element deposits in Australia: mineralogy, geochemistry and metallurgy. *Australian Journal of Earth Sciences* **2025**, *72*, 1005-1024, doi:10.1080/08120099.2025.2570934.
15. Löhr, S.C.; Spandler, C.; Baldermann, A. Controls on rapid rare earth element enrichment in sediments deposited by a continental-scale river system. *Geochimica et Cosmochimica Acta* **2024**, *366*, 48-64, doi:https://doi.org/10.1016/j.gca.2023.12.012.
16. Verplanck, P.L.; Mariano, A.N.; Mariano, A., Jr. Rare Earth Element Ore Geology of Carbonatites. *Rare Earth and Critical Elements in Ore Deposits* **2016**, *18*, 0, doi:10.5382/Rev.18.01.
17. Spandler, C.; Morris, C. Geology and genesis of the Toongi rare metal (Zr, Hf, Nb, Ta, Y and REE) deposit, NSW, Australia, and implications for rare metal mineralization in peralkaline igneous rocks. *Contributions to Mineralogy and Petrology* **2016**, *171*, doi:10.1007/s00410-016-1316-y.
18. Lottermoser, B.G. Rare-earth element mineralisation within the Mt. Weld carbonatite laterite, Western Australia. *Lithos* **1990**, *24*, 151-167, doi:https://doi.org/10.1016/0024-4937(90)90022-S.
19. Van Gosen, B.S.; Fey, D.L.; Shah, A.K.; Verplanck, P.L.; Hoefen, T.M. *Deposit model for heavy-mineral sands in coastal environments*; 2328-0328; US Geological Survey: 2014.
20. Mudd, G.M.; Jowitt, S.M. Rare earth elements from heavy mineral sands: Assessing the potential of a forgotten resource. *Applied Earth Science* **2016**, *125*, 107-113, doi:10.1080/03717453.2016.1194955.
21. Bamforth, T.G.; Xia, F.; Tiddy, C.J.; González-Álvarez, I.; Brugger, J.; Hu, S.-Y.; Schoneveld, L.E.; Pearce, M.A.; Putnis, A. High-Grade REE accumulation in regolith: Insights from supergene alteration of an apatite-rich vein at the Kapunda Cu mine, South Australia. *Mineralium Deposita* **2024**, 1-25.
22. Demol, J.; Ho, E.; Soldenhoff, K.; Senanayake, G. The sulfuric acid bake and leach route for processing of rare earth ores and concentrates: A review. *Hydrometallurgy* **2019**, *188*, 123-139, doi:https://doi.org/10.1016/j.hydromet.2019.05.015.
23. Li, Y.H.M.; Zhao, W.W.; Zhou, M.-F. Nature of parent rocks, mineralization styles and ore genesis of regolith-hosted REE deposits in South China: An integrated genetic model. *Journal of Asian Earth Sciences* **2017**, *148*, 65-95, doi:10.1016/j.jseaes.2017.08.004.
24. SKY Metals Ltd. ADDITIONAL RARE EARTH ELEMENT MINERALISATION AND DRILLING IMMINENT AT DORADILLA (5 April 2023). Available online: https://investorhub.skymetals.com.au/announcements/4344274 (accessed on 05/02/2024).
25. Poxon, R. Prospecting Licences 391–396, Midway prospect–via Bourke–N.S.W. Final relinquishment report. **1981**.
26. Freytag, I.; Thompson, R. Aberfoyle–Eastmet Doradilla Project N.S.W., Group progress report for the period 28 July 1980 to 27 January 1981. **1981**.
27. Young, C. Aberfoyle–Eastmet Doradilla Project, N.S.W. Project review & progress report for the period July 28, 1981 to January 27, 1982. **1982**.
28. Plimer, I.R. Malayaite and tin-bearing silicates from a skarn at Doradilla via Bourke, New South Wales. *Australian Journal of Earth Sciences* **1984**, *31*, 147-153, doi:10.1080/08120098408729286.
29. Byrnes, J. Bourke 1:250 000 Metallogenic Map SH/55-10: Metallogenic Study and Mineral Deposit Data Sheets; Geological Survey of New South Wales, Dept of Mineral Resources: Sydney, 1993.
30. Fergusson, C.L.; Fanning, C.; Phillips, D.; Ackerman, B. Structure, detrital zircon U–Pb ages and 40Ar/39Ar geochronology of the Early Palaeozoic Girilambone Group, central New South Wales: subduction, contraction and extension associated with the Benambran Orogeny. *Australian Journal of Earth Sciences* **2005**, *52*, 137-159.

 doi:10.20944/preprints202604.1504.v1

31. Gilmore, P.J.; Trigg, S.J.; Campbell, L.M. Coolabah 1:100 000 Geological Sheet 8235, 1st edition, Explanatory notes. *Geological Survey of New South Wales* **2018**, 88.
32. Burton, G. Petrological and geochemical evidence of metasomatism and the nature of the calcic progenitor rock at the Doradilla prospect, New South Wales; GS2015/1395; November 2015 2016.
33. Fraser, G.L.; Simpson, C.; Blevin, P.; Fitzherbert, J.; PJ, G.; Trigg, S.; Campbell, L.; Deyssing, L.; Greenfield, J.; Burton, G. *New SHRIMP U-Pb Zircon Ages from the Lachlan, Southern Thomson and New England Orogens, New South Wales: February 2011-June 2013*; Geoscience Australia: 2014.
34. Glen, R.; Saeed, A.; Hegarty, R.; Percival, I.; Bodorkos, S.; Griffin, W. Preliminary zircon data and tectonic framework for the Thomson Orogen, northwestern NSW. *GS Report* **2010**, *379*.
35. Yang, B.; Offler, R.; Fitzherbert, J.A.; Folkes, C.; Dwyer, R.; Clark, C. Basin provenance and its control on mineralisation within the Early Devonian Cobar Basin, western Lachlan Orogen, eastern Australia. *Australian Journal of Earth Sciences* **2024**, 1-20, doi:10.1080/08120099.2023.2290245.
36. Blevin, P.L. Petrological, Chemical and Metallogenic notes on the Granites of the Bourke 250k sheet, NSW; 2011.
37. Chappell, B.W.; White, A.J.R. Two contrasting granite types: 25 years later. *Australian Journal of Earth Sciences* **2001**, *48*, 489-499, doi:10.1046/j.1440-0952.2001.00882.x.
38. Burton, G.; Trigg, S.J.; Black, L. A Middle Triassic age for felsic intrusions and associated mineralisation in the Doradilla prospect area, New South Wales. *Quarterly Notes of the Geological Survey of New South Wales 125, 1-11* **2007**.
39. SKY Metals Ltd. LARGE-SCALE RARE EARTH ELEMENT MINERALISATION DISCOVERED AT DORADILLA (25 January 2023). Available online: https://investorhub.skymetals.com.au/announcements/4242995 (accessed on 05/02/2024).
40. Sun, Q. The Raman OH stretching bands of liquid water. *Vibrational Spectroscopy* **2009**, *51*, 213-217, doi:https://doi.org/10.1016/j.vibspec.2009.05.002.
41. Durickovic, I. Using Raman Spectroscopy for Characterization of Aqueous Media and Quantification of Species in Aqueous Solution. In *Applications of Molecular Spectroscopy to Current Research in the Chemical and Biological Sciences*, Stauffer, M.T., Ed.; IntechOpen: London, 2016.
42. Silva, E.N.; Ayala, A.P.; Guedes, I.; Paschoal, C.W.A.; Moreira, R.L.; Loong, C.K.; Boatner, L.A. Vibrational spectra of monazite-type rare-earth orthophosphates. *Optical Materials* **2006**, *29*, 224-230, doi:https://doi.org/10.1016/j.optmat.2005.09.001.
43. Clavier, N.; Mesbah, A.; Szenknect, S.; Dacheux, N. Monazite, rhabdophane, xenotime & churchite: Vibrational spectroscopy of gadolinium phosphate polymorphs. *Spectrochimica Acta Part A: Molecular and Biomolecular Spectroscopy* **2018**, *205*, 85-94, doi:https://doi.org/10.1016/j.saa.2018.07.016.
44. Ondrejka, M.; Bačík, P.; Sobocký, T.; Uher, P.; Škoda, R.; Mikuš, T.; Luptáková, J.; Konečný, P. Minerals of the rhabdophane group and the alunite supergroup in microgranite: products of low-temperature alteration in a highly acidic environment from the Velence Hills, Hungary. *Mineralogical Magazine* **2018**, *82*, 1277-1300, doi:10.1180/mgm.2018.137.
45. Batch, T.; Tiddy, C.; Brotodewo, A.; Giles, D.; Little, G.; Belperio, A.; Taylor, M.; Metelka, V. REE-bearing phosphate mineral chemistry for iron sulfide-copper-gold exploration: A study at Jericho, NW Queensland, Australia. *Journal of Geochemical Exploration* **2024**, *267*, doi:10.1016/j.gexplo.2024.107608.
46. Linthout, K. Tripartite division of the system 2REEPO~ 4-CaTh (PO~ 4)~ 2-2ThSiO~ 4, discreditation of brabantite, and recognition of cheralite as the name for members dominated by CaTh (PO~ 4)~ 2. *Canadian Mineralogist* **2007**, *45*, 503.
47. Ondrejka, M.; Uher, P.; Pršek, J.; Ozdín, D. Arsenian monazite-(Ce) and xenotime-(Y), REE arsenates and carbonates from the Tisovec-Rejkovo rhyolite, Western Carpathians, Slovakia: Composition and substitutions in the (REE,Y)XO4 system (X = P, As, Si, Nb, S). *Lithos* **2007**, *95*, 116-129, doi:https://doi.org/10.1016/j.lithos.2006.07.019.
48. Williams, M.L.; Jercinovic, M.J.; Hetherington, C.J. Microprobe monazite geochronology: understanding geologic processes by integrating composition and chronology. *Annu. Rev. Earth Planet. Sci.* **2007**, *35*, 137-175.

 doi:10.20944/preprints202604.1504.v1

49. Hetherington, C.J.; Jercinovic, M.J.; Williams, M.L.; Mahan, K. Understanding geologic processes with xenotime: Composition, chronology, and a protocol for electron probe microanalysis. *Chemical Geology* **2008**, *254*, 133-147, doi:https://doi.org/10.1016/j.chemgeo.2008.05.020.
50. Walsh, J.M.J.; Spandler, C. The role of zircon in hydrothermal heavy REE mineralisation: The case for unconformity-related ore deposits of north-west Australia. *Chemical Geology* **2023**, *629*, 121493, doi:https://doi.org/10.1016/j.chemgeo.2023.121493.
51. Förster, H.J. Composition and origin of intermediate solid solutions in the system thorite–xenotime–zircon–coffinite. *Lithos* **2006**, *88*, 35-55, doi:https://doi.org/10.1016/j.lithos.2005.08.003.
52. Bau, M.; Schmidt, K.; Koschinsky, A.; Hein, J.; Kuhn, T.; Usui, A. Discriminating between different genetic types of marine ferro-manganese crusts and nodules based on rare earth elements and yttrium. *Chemical Geology* **2014**, *381*, 1-9, doi:https://doi.org/10.1016/j.chemgeo.2014.05.004.
53. Takahashi, Y.; Manceau, A.; Geoffroy, N.; Marcus, M.A.; Usui, A. Chemical and structural control of the partitioning of Co, Ce, and Pb in marine ferromanganese oxides. *Geochimica et Cosmochimica Acta* **2007**, *71*, 984-1008, doi:https://doi.org/10.1016/j.gca.2006.11.016.
54. Knorsch, M.; Gazley, M.; Ince, M.; Kartal, M.; Trunfull, E.; Lilly, K.; Piechocka, A. An introduction to clay-hosted REE deposits in Australia. *Geoscience Frontiers* **2025**, *16*, doi:10.1016/j.gsf.2024.101977.